Supplementary Figures

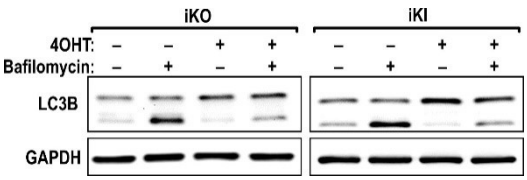

Fig. S1. Autophagy flux was inhibited to similar degrees in FIP200 KO and FIP200 KI PyMT cells. Immunoblots showing levels of LC3B and GAPDH in iKO and iKI tumor cells ± 4OHT treatment. In Bafilomycin A1 treated conditions, cells were treated for 2 hours with 200nM of bafilomycin.

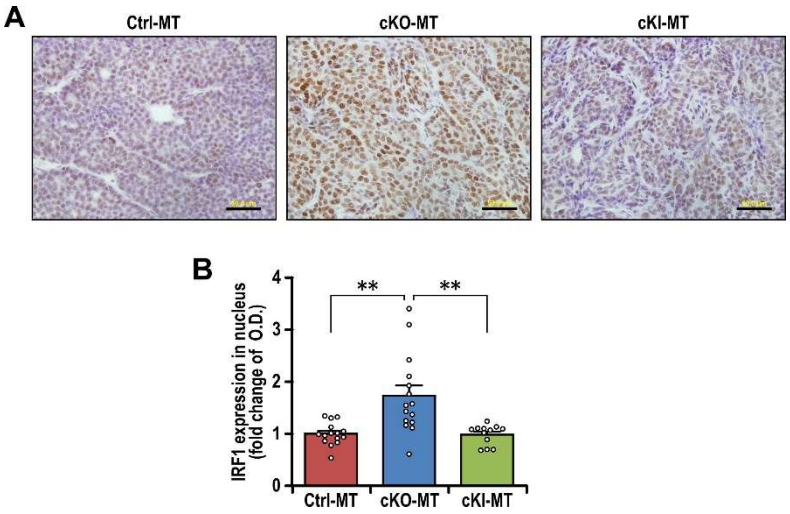

Fig. S2. Increased accumulation of nuclear IRF1 in cKO-MT tumors but not cKI-MT tumors, relative to Ctrl-MT tumors. **(A)** Immuno-histochemical analysis of IRF1 in Ctrl-MT, cKO-MT and cKI-MT tumors. Scale bar represents 50µm. **(B)** Quantification of optical density for IRF1 staining in Ctrl-MT, cKO-MT and cKI-MT tumors. Statistical significance was determined by Kruskal-Wallis test with Dunn's test, ** denotes $p \leq 0.01$.

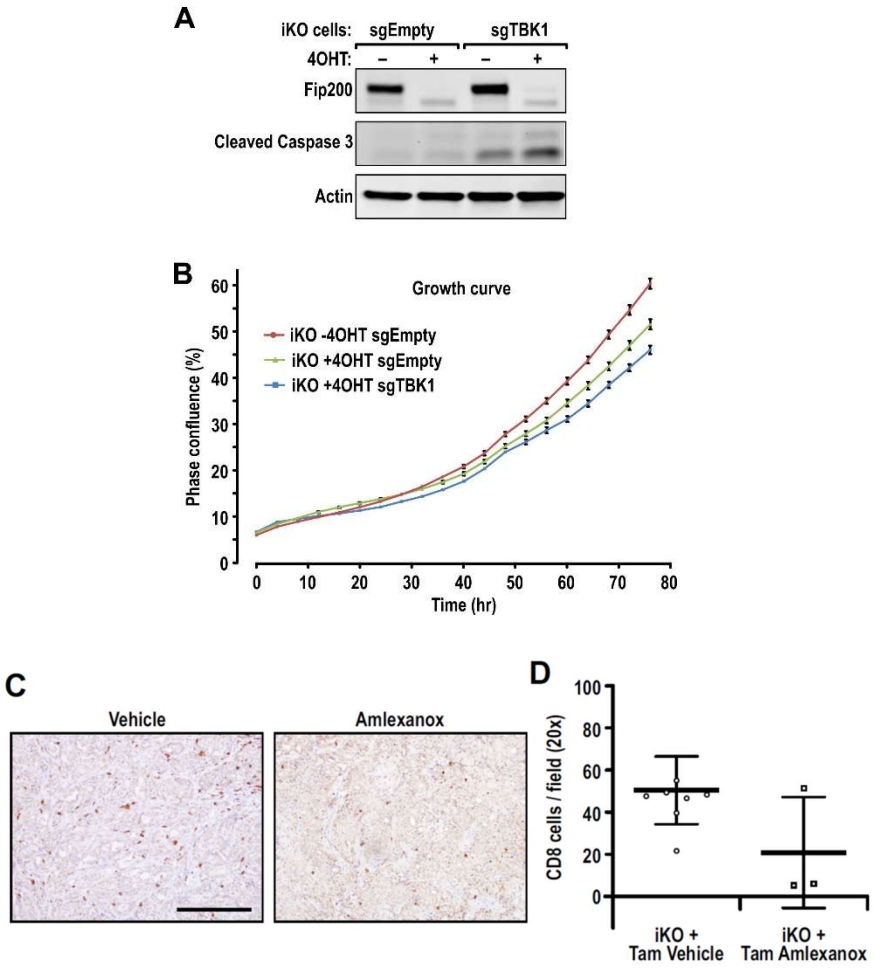

Fig. S3. Genetic depletion of TBK1 increased cleaved-caspase 3 levels in PyMT cells. **(A)** Immunoblots showing levels of FIP200, cleaved-caspase 3 and Actin in iKO cells transduced with sgEmpty or sgTBK1, ± 4OHT treatment. **(B)** Graph showing confluency of cells across time for iKO cells transduced with sgEmpty or sgTBK1, ± 4OHT treatment. (**C)** Representative images of iKO (+Tam) vehicle control and iKO (+Tam) amlexanox treated tumors immuno-stained for CD8. Scale bar represents 50µm. (**D)** Bar chart showing quantification of CD8 positive cells per field of view in iKO (+Tam) tumors (vehicle control; n=9, amlexanox; n=3 mice).

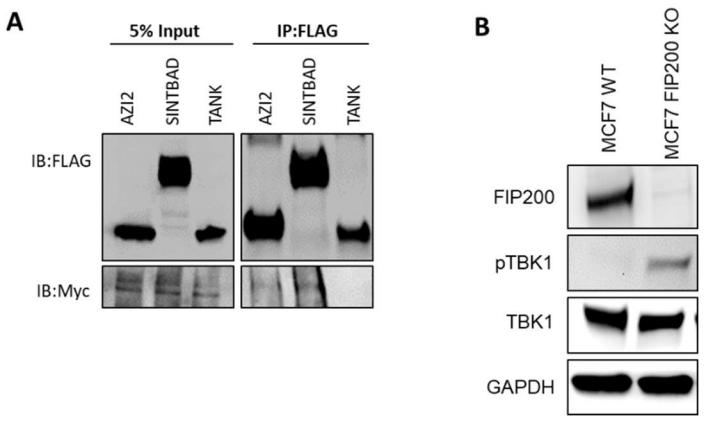

Fig. S4. Interaction between FIP200 and TBK1 adaptors and activation of TBK1 upon FIP200 ablation. **(A)** Immunoblots of co-IP experiments with FLAG antibody, in HEK293 cells transfected with either HA/FLAG-AZI2, HA/FLAG-SINTBAD or FLAG-TANK along with MYC-FIP200. **(B)** Immunoblots showing the levels of FIP200, p-TBK1, TBK1 and GAPDH in MCF7 WT (sgEmpty) and MCF7 FIP200KO (sgFIP200) cells.

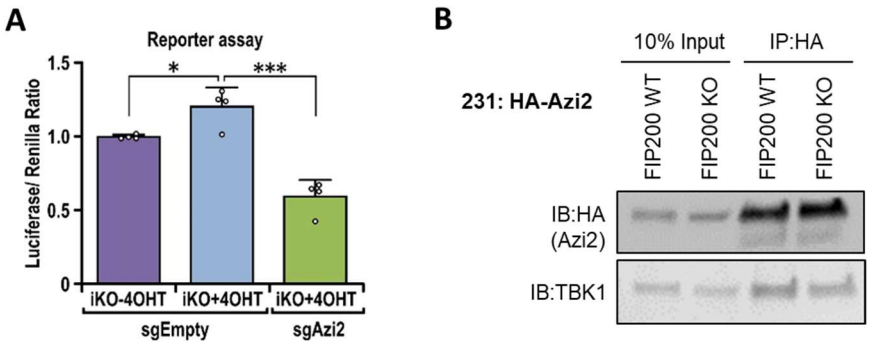

Fig. S5. Genetic depletion of AZI2 in iKO (+4OHT) cells diminished the increase in ISG56-reporter activity upon FIP200 ablation and loss of FIP200 does not increase the interaction between AZI2 and TBK1. (**A)** Bar charts showing luciferase/renilla luminescence ratios in iKO (-4OHT) sgEmpty, iKO (+4OHT) sgEmpty and iKO (+4OHT) sg AZI2 cells. Statistical significance was determined by ANOVA followed by Tukey's test, * denotes $p \leq 0.05$, *** denotes $p \leq 0.001$. **(B)** Immunoblots of co-IP experiments with HA antibody, in MDA-MB-231 WT or FIP200 KO cells transfected with HA/FLAG-AZI2.

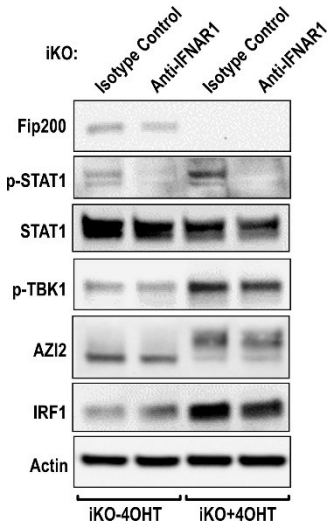

Fig. S6. Levels of TBK1 activation and AZI2 phosphorylation upon IFNAR1 blockade in FIP200 ablated cells. Immunoblots showing levels of FIP200, p-STAT1, STAT1, p-TBK1, AZI2, IRF1 and ACTIN in iKO cells (± 4OHT), treated with 10µg/ml isotype control antibody or anti-IFNAR1 antibody for 24 hours.

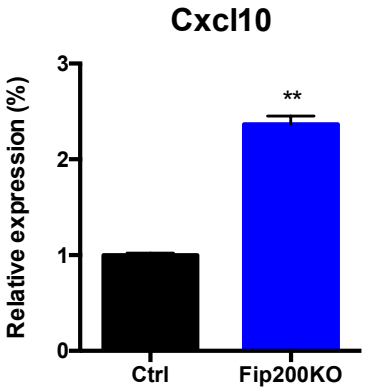

Fig. S7. Increased expression of CXCL10 in MDA-MB-231 human breast cancer cells upon ablation of FIP200. Bar chart showing levels of CXCL10 as determined by quantitative-PCR in Ctrl and FIP200 KO MDA-MB-231 cells. Statistical analysis was determined by t-test, ** denotes $p \leq 0.01$.

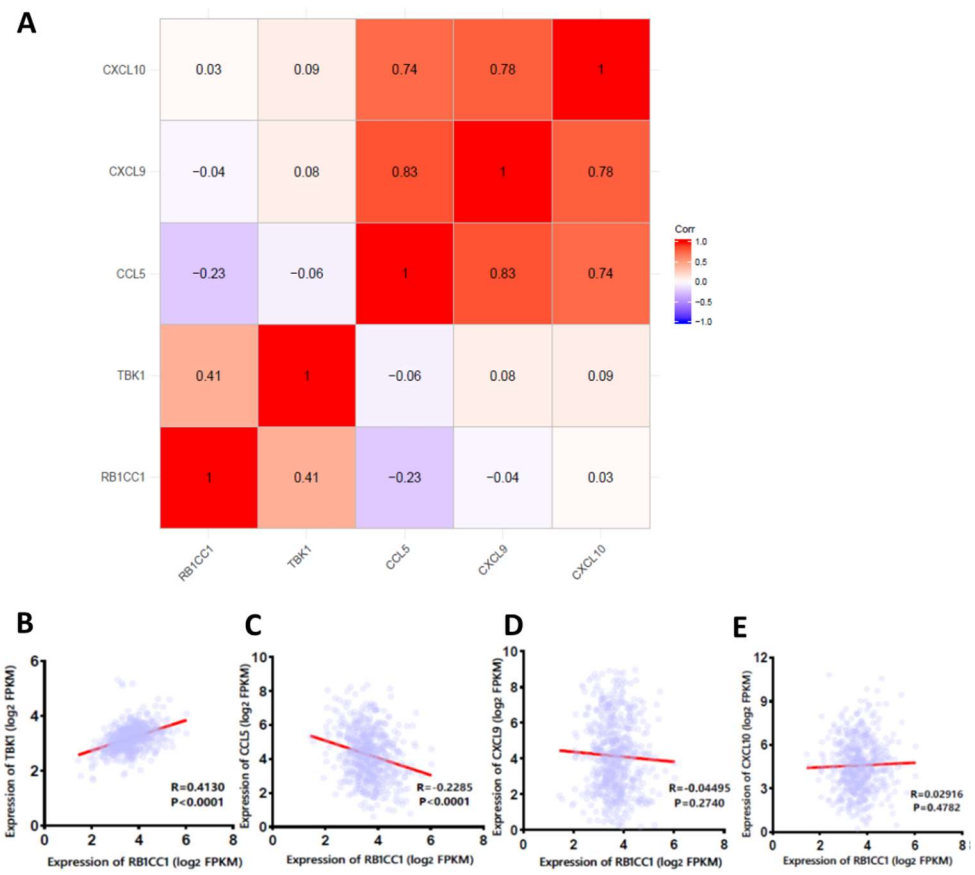

Fig. S8. Analysis of chemokine, FIP200 (RB1CC1) and TBK1 levels in breast cancers from the TCGA cohort. **(A)** Correlation matrix for Pearson's test of RB1CC1, TBK1, CCL5, CXCL9 and CXCL10. Scatter plots showing correlation among the expression of RB1CC1 with either **(B)** TBK1, **(C)** CCL5, **(D)** CXCL9 or **(E)** CXCL10. The correlation was calculated by Pearson correlation coefficient and Z-test, and the expression value was Log2 transformed.